Diffusive transport of light in a Kelvin foam

MirFaez Miri,[1] Ebrahim Madadi,[1] and Holger Stark[2]
[1]*Institute for Advanced Studies in Basic Sciences, Zanjan, 45195-1159, Iran*
[2]*Universität Konstanz, Fachbereich Physik, D-78457 Konstanz, Germany*
(Received 22 May 2005; published 28 September 2005)

Although diffusing-wave spectroscopy has already been successfully applied to study dynamic properties of foams, we still lack a clear understanding of the diffusive transport of photons in foams. In this paper, we present a thorough study of photon diffusion in the Kelvin structure as an example for a three-dimensional model foam. We consider the photons' random walk as they are reflected or transmitted by the liquid films according to the rules of ray optics. For constant reflectance and special one- and two-dimensional photon paths, we are able to calculate diffusion constants analytically. Extensive numerical simulations reveal a remarkable similarity with our previous two-dimensional investigations. To implement a more realistic model, we use thin-film reflectances. The simulated diffusion constants exhibit oscillations for varying film thickness d which vanish when disorder is introduced in d. Absolute values and the behavior at small d agree with measurements in very dry foams providing a strong argument for the importance of liquid films in the diffusive photon transport. An analytical theory with a minimum of input parameters reproduces the numerical results.

DOI: 10.1103/PhysRevE.72.031111 PACS number(s): 05.40.Fb, 05.60.−k, 82.70.Rr, 42.25.Dd

I. INTRODUCTION

Many objects in nature, e.g., conventional colloidal suspensions or thick aligned nematic liquid crystals, are visibly opaque. In such turbid samples, each photon is scattered many times before exiting the material. Therefore the photon can be considered as a random walker which ultimately leads to a diffusive transport of light intensity [1–3]. Diffusing-wave spectroscopy (DWS) [4,5] and diffuse-transmission spectroscopy (DTS) [6] exploit the diffusive nature of light transport to provide information about the static and dynamic properties of an opaque system.

Recent experiments have applied diffusing-wave spectroscopy to cellular structures such as foams which consist of air bubbles separated by liquid films [7–14]. This suggests that the model for photon transport based on the random walk picture is still valid. However, the mechanisms underlying the random walk are not well understood. A relatively dry foam consists of cells separated by thin liquid films. Three of them meet in the so-called Plateau borders which then define tetrahedral vertices [15]. One suggestion is that light scattering from the Plateau borders is responsible for the random walk [9]. The transport-mean-free path l^* over which the photon direction becomes randomized is then predicted as $l^* \propto H/\sqrt{\epsilon}$, where H is the average bubble diameter and ϵ is the liquid volume fraction. However, data rule this out in favor of the empirical law $l^* \approx H(0.14/\epsilon + 1.5)$ [9]. This may imply significant scattering from vertices [16] or films [17–19]. New questions about the role of Plateau borders are raised by recent experiments on the absorption of diffuse photons in an aqueous foam due to a dye added to the liquid phase [20]. The absorption is large in the intermediate wetness range $0.04 < \epsilon < 0.2$ and reaches its maximum at $\epsilon \approx 0.07$. This encourages novel transport effects, such as total internal reflection of photons inside the Plateau borders [20]. Apparently, the role of Plateau borders, vertices, and films for light transport in foams beg for complete theoretical understanding.

We concentrate on the role of liquid films to study light transport in dry foams. Cells in a foam are much larger than the wavelength of light, thus one can employ ray optics and follow a light beam or photon as it is reflected by the liquid films with a probability r called the intensity reflectance. This naturally leads to a persistent random walk of the photons, where the walker remembers its direction from the previous step [21,22]. First introduced by Fürth as a model for diffusion in a number of biological problems [23], and shortly after by Taylor in the analysis of turbulent diffusion [24], the persistent random walk model is now applied to a multitude of diverse problems and systems such as polymers [25], diffusion in solids [26], dispersal of spores [27], cell movement [28], and general transport mechanisms [29–31].

We have already studied photon transport in *two-dimensional* foams. We started with the simplest model, the regular honeycomb structure, using a constant intensity reflectance r. We found a rich behavior of the diffusion constant in terms of the possible photon paths and reflectance [17]. The honeycomb structure is highly idealistic, therefore we extended our studies towards real dry foams in two steps [18]. In a first model, we introduced topological and geometrical disorder based on a Voronoi foam model [32,33] to investigate the influence of disorder. The essential result of our Monte Carlo simulations is summarized in the empirical formula for the diffusion constant $D(r)$,

$$D_{\text{Voronoi}}(r) = 0.25Hc\frac{1-r}{r}(1 - b_1 + b_2 r). \tag{1}$$

The main behavior is governed by the first factor on the right-hand side, which is also found in the honeycomb structure. However, there is a small but systematic deviation from it described by the last factor with $0 < b_1 < 0.1$ and $b_2 \approx 0.1$. Both constants show a clear dependence on disorder in the Voronoi foam [18,19]. In a second model, we used the intensity reflectance of thin films with its significant dependence

on the incident angle and on d/λ, where d is film thickness and λ the wavelength of light. We found that l^*/H increases with decreasing film thickness for $d/\lambda < 0.2$ and that it varies between 2 and 12, where the last value applies to a common black film with $d \approx 30$ nm [15]. Our results agree with measurements by Vera *et al.* where l^*/H increases from 2 to 20 for decreasing ε [9]. This quantitative agreement serves as a first strong argument for the importance of liquid films in the diffusive transport, otherwise they should result in much larger transport mean free paths.

In this paper, we extend our studies towards real *three-dimensional* dry foams to explore the effect of space dimension on the photon transport. Inspired by the success of a regular honeycomb in two dimensions, we choose the Kelvin structure as a three-dimensional model foam [15] but ignore curvature of the liquid films. Although periodic in space, the Kelvin structure has been used for analytic access to the physical properties of foams as exemplified by work on their rheological behavior [34]. In the Kelvin structure, we will identify special one- and two-dimensional photon paths. For one random-walk type taking place on a square-rectangle tiling, we are able to evaluate the diffusion constant analytically although it corresponds to a Markov chain of eighth order. The calculations are done based on the model of constant intensity reflectance, for which we then present extensive numerical studies of photon diffusion in the full three-dimensional space. They reveal a remarkable universality of Eq. (1). In order to treat a more realistic model, we use the intensity reflectances of thin films within our Monte Carlo simulations as in the two-dimensional case. The numerical results show oscillations in the diffusion constant when plotted as a function of d/λ which, however, vanish when we introduce disorder in the film thickness. Absolute values of l^*/H are in agreement with measurements for very dry foams. This confirms our conclusion from the previous paragraph that liquid films are important for the diffusive transport of light. We will, furthermore, present an analytical theory with which we are able to reproduce our numerical results. It only needs a minimum of input parameters and the angular distribution function of the photons.

Our paper is organized as follows. In Sec. II we introduce the possible photon paths in a Kelvin structure and identify special cases. Photon transport in a Kelvin structure using constant and thin-film intensity reflectances are discussed in Secs. III and IV, respectively. We close with a discussion of our results and conclusions in Sec. V.

II. PHOTON PATHS IN THE KELVIN STRUCTURE

Kelvin's structure is a three-dimensional periodic foam that consists of tetrakaidecahedra (14-sided cells) in the bcc arrangement. The Kelvin cell is similar to the Wigner-Seitz cell of the bcc lattice, with some subtle curvature of the faces, in order to satisfy the equilibrium rules of Plateau [15]. Proposed by Kelvin to partition space into equal-volume cells with the least interface area, it is now known that the Weaire-Phelan structure is a better solution to this problem [35–37].

As a simplification, we consider a tetrakaidecahedron with flat surfaces (see Fig. 1). It has six square and eight hexagonal faces, with an edge length l. As shown in Appendix A, the volume of the tetrakaidecahedron is equal to the volume of a sphere of diameter

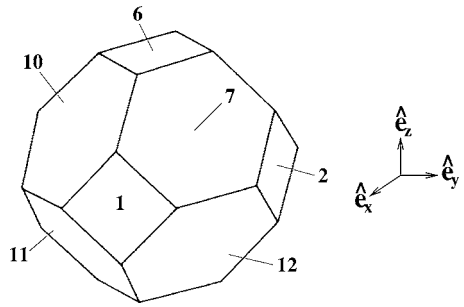

FIG. 1. The tetrakaidecahedral cell with flat surfaces. Note that the squares 3, 4, and 5 lie opposite to the respective squares 1, 2, and 6; the hexagons 8, 9, 13, and 14 lie opposite to the respective hexagons 11, 12, 10, and 7.

$$H = \sqrt[3]{\frac{48\sqrt{2}}{\pi}}\, l \approx 2.78528 l. \tag{2}$$

As a comparison, the distances between opposite square and hexagonal faces are $2\sqrt{2}l \approx 2.82843l$ and $\sqrt{6}l \approx 2.44949l$, respectively. We choose a Cartesian coordinate system whose origin is placed at the center of the unit cell and whose base vectors $\hat{\boldsymbol{e}}_x$, $\hat{\boldsymbol{e}}_y$, and $\hat{\boldsymbol{e}}_z$ point along the respective surface normals of the faces 1, 2, and 6 (see Fig. 1). For the ith face, the normal vector $\hat{\boldsymbol{n}}_i$, center $\boldsymbol{c}_i$, and vertices $\boldsymbol{v}_i^j$ ($1 \leqslant j \leqslant 4$ for the square faces and $1 \leqslant j \leqslant 6$ for the hexagonal faces) are reported in Appendix A.

In the following, we model the photon paths in a Kelvin structure as a random walk with rules motivated by ray optics, i.e., an incoming light beam is reflected from a face with a probability r, called intensity reflectance, or traverses the face with a probability $t = 1 - r$, called transmittance. We assume that the faces (films) are infinitely thin so there is no lateral displacement of the transmitted light ray along the face. In the concrete calculations, we will normalize edge length l and light velocity c to 1.

First, we consider photon paths in a tetrakaidecahedron with completely reflecting faces ($r = 1$). A photon propagating in the direction of unit vector $\hat{\boldsymbol{V}}$ and being reflected from the ith face moves along a new direction given by unit vector

$$\hat{\boldsymbol{V}}_{\boldsymbol{r}} = \hat{\boldsymbol{V}} - 2\hat{\boldsymbol{n}}_i(\hat{\boldsymbol{V}} \cdot \hat{\boldsymbol{n}}_i). \tag{3}$$

It satisfies $\hat{\boldsymbol{V}}_{\boldsymbol{r}} \times \hat{\boldsymbol{n}}_i = \hat{\boldsymbol{V}} \times \hat{\boldsymbol{n}}_i$ and $\hat{\boldsymbol{V}}_{\boldsymbol{r}} \cdot \hat{\boldsymbol{n}}_i = -\hat{\boldsymbol{V}} \cdot \hat{\boldsymbol{n}}_i$, i.e., $\hat{\boldsymbol{V}}_{\boldsymbol{r}}$, $\hat{\boldsymbol{n}}_i$, and $\hat{\boldsymbol{V}}$ are coplanar and the angle of reflection equals the angle of incidence. In general, a photon path is embedded in three-dimensional space. *One-dimensional* and *two-dimensional* photon paths in a tetrakaidecahedral billiard deserve attention, since they are not expected in asymmetric and nonregular billiards. From the geometry and symmetry of a tetrakaidecahedron, it follows immediately that perpendicular incidence on the faces leads to one-dimensional photon paths. There are three of them for the square and four for the hexagonal faces. For a two-dimensional path, all incidence and reflection directions have to be in the same plane of

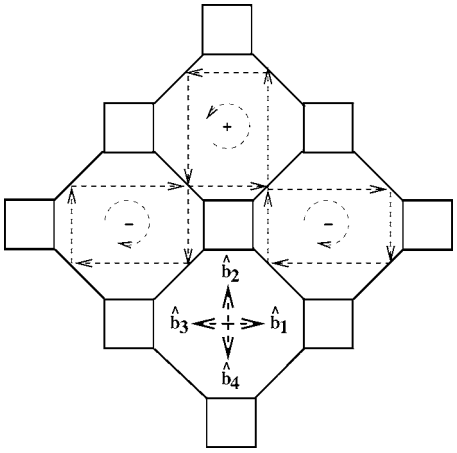

FIG. 2. Path of photons injected in the plane $z=0$ with an angle of 45° relative to a long edge of an octagon. Note that the intersection of the plane $z=0$ with the Kelvin structure is a tiling of octagons and squares. The photons move along four directions $\hat{\boldsymbol{b}}_1$, $\hat{\boldsymbol{b}}_2$, $\hat{\boldsymbol{b}}_3$, and $\hat{\boldsymbol{b}}_4$ with a short and a long step length. By transmission to a neighboring cell, the helicity of the photon path changes.

motion specified by the normal vector $\hat{\boldsymbol{N}}$, i.e., $\hat{\boldsymbol{N}}\cdot\hat{\boldsymbol{V}}=\hat{\boldsymbol{N}}\cdot\hat{\boldsymbol{V}}_r=0$. Equation (3) then implies that the normal vectors of all reflecting faces should be in the plane of motion, i.e., $\hat{\boldsymbol{N}}\cdot\hat{\boldsymbol{n}}_i=0$. As an example, photons will not leave the plane characterized by $x=y$ (it cuts the faces 5, 6, 7, 9, 12, and 14) since all their normal vectors lie in the plane of motion. A detailed analysis of the condition $\hat{\boldsymbol{N}}\cdot\hat{\boldsymbol{n}}_i=0$ shows that planar motion only occurs in planes characterized by $x=\pm y-h_0$, $x=\pm z-h_0$, and $y=\pm z-h_0$, where $-\sqrt{2}l/2\leqslant h_0\leqslant\sqrt{2}l/2$. Furthermore, the normal vectors of square faces lie in the $x=h_0$, $y=h_0$, and $z=h_0$ planes giving planar photon paths where reflections from hexagonal faces are excluded.

The intersection of the $x=y-h_0$ plane (and its symmetry related ones) with the space filling Kelvin structure is a distorted hexagonal tessellation. Each hexagon has two edges of length l and four edges of length $\sqrt{3}l$. The intersection of the $z=h_0$ plane with the Kelvin structure is a tiling of octagons and squares (see Fig. 2 for $h_0=0$). Each octagon has four edges of length $l+\sqrt{2}|h_0|$ and four edges of length $\sqrt{2}l-2|h_0|$. The edge length of the squares is $l+\sqrt{2}|h_0|$. For a special injection angle of 45° relative to a long edge of an octagon, photons move along a closed path. They, therefore, allow an analytical treatment of the random walk which takes place at intensity reflectances $r<1$. We will illustrate the calculation of the corresponding diffusion constants in the following section.

III. PHOTON TRANSPORT IN A KELVIN STRUCTURE: MODEL OF CONSTANT INTENSITY REFLECTANCE

A. Analytical treatment of 1D and 2D transport

As already mentioned in the Introduction, the random walk in a Kelvin structure based on ray optics is a persistent random walk since the new direction chosen by the photon in the $n+1$th step depends on the direction of the nth step. In one dimension, which in our case corresponds to perpendicular incidence on the faces, the solution for the probability $P_n(x)$ of finding the random walker at location x after n steps is well-known. It is determined in the framework of master equations and characteristic functions, i.e., the spatial Fourier transforms of probability distributions [21]. The persistent walk in one dimension is a second-order Markov process since $P_n(x)$ obeys a second-order linear difference equation in the discrete step index n which, in the continuous case, gives the telegrapher equation. For both equations, the long-time limit is shown to be diffusive. In our case, with step length $2\sqrt{2}l$ between opposite square faces and $\sqrt{6}l$ between opposite hexagonal faces

$$D(\hat{\boldsymbol{n}}_1)=D(\hat{\boldsymbol{n}}_2)=D(\hat{\boldsymbol{n}}_5)=\sqrt{2}\frac{1-r}{r}lc,$$

$$D(\hat{\boldsymbol{n}}_7)=D(\hat{\boldsymbol{n}}_8)=D(\hat{\boldsymbol{n}}_9)=D(\hat{\boldsymbol{n}}_{10})=\frac{\sqrt{6}}{2}\frac{1-r}{r}lc, \qquad (4)$$

where $D(\hat{\boldsymbol{n}}_i)$ is the diffusion constant for photons launched along the surface normal $\hat{\boldsymbol{n}}_i$.

The analytical treatment of the two-dimensional transport is much more elaborate. At the end of Sec. II, we identified for totally reflecting faces a closed photon path in the $z=0$ plane, where the photon is reflected from one square face to the other under an injection angle of 45° (see Fig. 2). The photon path consists of four steps along the unit vectors $\hat{\boldsymbol{b}}_1$, $\hat{\boldsymbol{b}}_2$, $\hat{\boldsymbol{b}}_3$, and $\hat{\boldsymbol{b}}_4$. Now, for partially reflecting faces ($r<1$), photons perform a two-dimensional random walk in the tiling of octagons and squares in the $z=0$ plane as indicated in Fig. 2.

To treat the two-dimensional random walk analytically, it is necessary to identify different photon states. According to Fig. 2, the photon in the rightmost (leftmost) cell is reflected to the right. When it moves to the neighboring cell with a probability $t=1-r$, its attribute to be reflected to the right changes and it is reflected to the left. Therefore, to fully characterize the status of a photon, we have to introduce a helicity $\pm$ besides the position and the step vectors. In addition, after transmission to a neighboring cell, the step vectors along one direction interchange their lengths (see Fig. 2). We take this into account by introducing separate step vectors $\boldsymbol{b}_i^+$ and $\boldsymbol{b}_i^-$. The magnitude of the long and short steps are $l(1+2f)$ and $l(3-2f)$, respectively, where $\sqrt{2}fl$ ($0\leqslant f\leqslant 1$) is the starting position on the long edge of an octagon. The average step length is thus $2l$, and it is assumed for $f=0.5$ where the photon path is composed of equal steps.

We denote by $P_n^{\pm i}(\boldsymbol{x})$ the probability that the photon after its nth step arrives at position $\boldsymbol{x}=(x,y)$ with step vector $\boldsymbol{b}_i^{\pm}$ and helicity $\pm$. According to Fig. 2, we can establish a set of eight master equations which couple the probabilities at step $n+1$ to the probabilities at step n. We only give the first four equations:

$$P_{n+1}^{+1}(\boldsymbol{x})=rP_n^{+4}(\boldsymbol{x}-\boldsymbol{b}_1^+)+tP_n^{-1}(\boldsymbol{x}-\boldsymbol{b}_1^+),$$

$$P_{n+1}^{-1}(\boldsymbol{x})=rP_n^{-2}(\boldsymbol{x}-\boldsymbol{b}_1^-)+tP_n^{+1}(\boldsymbol{x}-\boldsymbol{b}_1^-),$$

$$P_{n+1}^{+2}(\boldsymbol{x}) = rP_n^{+1}(\boldsymbol{x}-\boldsymbol{b}_2^+) + tP_n^{-2}(\boldsymbol{x}-\boldsymbol{b}_2^+),$$

$$P_{n+1}^{-2}(\boldsymbol{x}) = rP_n^{-3}(\boldsymbol{x}-\boldsymbol{b}_2^-) + tP_n^{+2}(\boldsymbol{x}-\boldsymbol{b}_2^-). \quad (5)$$

For the description of the photon distribution in the plane, we do not need to specify the internal state (helicity, step vector) explicitly. That means we are mainly interested in the probability that the photon arrives at position $\boldsymbol{x}$ at step n,

$$P_n(\boldsymbol{x}) = \sum_{\pm,i} P_n^{\pm i}(\boldsymbol{x}). \quad (6)$$

For $P_n(\boldsymbol{x})$, we determine the first and second moments as the characteristic features of a random walk:

$$\langle x\rangle_n = \int\int xP_n(x,y)dxdy,$$

$$\langle y\rangle_n = \int\int yP_n(x,y)dxdy,$$

$$\langle (x-\langle x\rangle_n)^2\rangle_n = \int\int (x-\langle x\rangle_n)^2P_n(x,y)dxdy,$$

$$\langle (y-\langle y\rangle_n)^2\rangle_n = \int\int (y-\langle y\rangle_n)^2P_n(x,y)dxdy. \quad (7)$$

Using the Fourier transform of the probability distribution, also called characteristic function,

$$P_n(\boldsymbol{k}) = \int\int e^{i\boldsymbol{k}\cdot\boldsymbol{x}}P_n(x,y)dxdy, \quad (8)$$

the moments are conveniently calculated:

$$\langle x^{m_1}y^{m_2}\rangle = (-i)^{m_1+m_2}\frac{\partial^{m_1+m_2}P_n(\boldsymbol{k})}{\partial k_x^{m_1}\partial k_y^{m_2}}\bigg|_{\boldsymbol{k}=\boldsymbol{0}}, \quad (9)$$

where $\boldsymbol{k}=(k_x,k_y)$ and m_1, m_2 are positive integers including zero.

We apply the formalism developed in Ref. [17] and find that $P_n(\boldsymbol{k})$ satisfies

$$\sum_{i=0}^{i=4} m_{2i}P_{n+2i}(\boldsymbol{k}) = 0, \quad (10)$$

where

$$m_8 = 1,$$

$$m_6 = -(1-r)^2\sigma_1,$$

$$m_4 = 2(1-2r)(1+2r^2-2r) + (1-2r)(1-r)^2\sigma_2,$$

$$m_2 = -(1-r)^2(1-2r)^2\sigma_1,$$

$$m_0 = (1-2r)^4,$$

$$\sigma_1 = 2\cos[\boldsymbol{k}\cdot(\boldsymbol{b}_1^+ + \boldsymbol{b}_1^-)] + 2\cos[\boldsymbol{k}\cdot(\boldsymbol{b}_2^+ + \boldsymbol{b}_2^-)],$$

$$\sigma_2 = 2\cos[\boldsymbol{k}\cdot(\boldsymbol{b}_1^+ + \boldsymbol{b}_1^- + \boldsymbol{b}_2^+ + \boldsymbol{b}_2^-)] + 2\cos[\boldsymbol{k}\cdot(\boldsymbol{b}_1^+ + \boldsymbol{b}_1^- - \boldsymbol{b}_2^+ - \boldsymbol{b}_2^-)]. \quad (11)$$

Note that Eq. (10) is an eighth-order linear difference equation for $P_n(\boldsymbol{k})$, indicating that the corresponding random walk is an eighth-order Markov chain. In the continuum limit, it would correspond to a linear partial differential equation with time derivatives up to the eighth order.

We do not make an attempt to determine $P_n(\boldsymbol{k})$ completely. Instead we are interested in the long-time limits of its first two moments. Taking first derivatives of Eq. (10) with respect to $\boldsymbol{k}$ and using Eq. (9), we find a master equation for the mean displacement along the x direction

$$\sum_{i=0}^{i=4} m_{2i}|_{\boldsymbol{k}=0}\langle x\rangle_{n+2i} = 0 \quad (12)$$

and the equivalent result for the y direction. To arrive at Eq. (12), we used $\partial m_{2i}/\partial\boldsymbol{k}|_{\boldsymbol{k}=\boldsymbol{0}}=\boldsymbol{0}$. To solve Eq. (12), we insert the ansatz $\langle x\rangle_n \propto z^n$, and find that $z \in [\pm 1, \pm\sqrt{1-2r}, \pm\sqrt{1-2r}, \pm(1-2r)]$. The magnitude of each z is smaller than or equal to one. We can therefore conclude that in the long-time limit or for large n

$$\langle x\rangle_n = \langle y\rangle_n = 0. \quad (13)$$

The mean-square displacement along x obeys

$$\sum_{i=0}^{i=4}\left(m_{2i}|_{\boldsymbol{k}=\boldsymbol{0}}\langle x^2\rangle_{n+2i} - \frac{\partial^2 m_{2i}}{\partial k_x^2}\bigg|_{\boldsymbol{k}=\boldsymbol{0}}\right) = 0, \quad (14)$$

an equivalent equation is valid along y. Note that Eq. (14) corresponds to Eq. (12) but now with an inhomogeneity. Since we already know the solutions of the homogeneous equation, they decay to zero or give a constant of the order of one in the long-time limit, we just need a special solution for which we make the ansatz $\langle x^2\rangle_n = a_0 n$. The constant a_0 is easily found from Eq. (14) and we obtain in the long-time limit

$$\langle x^2\rangle_n = \frac{1}{S_2}\frac{\partial^2 S_1}{\partial k_x^2}\bigg|_{\boldsymbol{k}=\boldsymbol{0}} n, \quad (15)$$

where $S_1=\Sigma_{i=1}^{i=3} m_{2i}$ and $S_2=\Sigma_{i=1}^{i=4} 2im_{2i}$. For sufficiently large values of n, the time for n steps is $\tau = 2\,ln/c$, where $2l$ is the average step length. Returning to physical units, we obtain the diffusive behavior of the mean-square displacements

$$\langle x^2\rangle = 2D_x\tau \text{ and } \langle y^2\rangle = 2D_y\tau, \quad (16)$$

where the diffusion constants read

$$D_x = D_y = \frac{1-r}{r}lc. \quad (17)$$

As expected, the planar diffusion is isotropic. Note that although the single step lengths depend on the starting position on the edge of an octagon, only their average appears in the final result. Note further that all our arguments can be extended to planes characterized by $z=h_0(-\sqrt{2}l/2 \leqslant h_0 \leqslant \sqrt{2}l/2)$, where the same type of random walk occurs. Finally, our analytical results of Eqs. (4) and (17) also provide

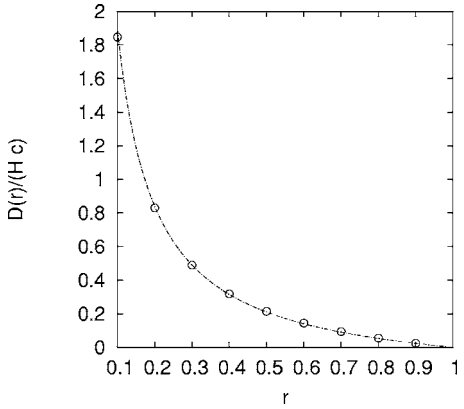

FIG. 3. The diffusion constant in units of cell diameter H times light velocity c as a function of intensity reflectance r. $D(r)/(Hc) = 0.21(1-r)/r$ and Monte Carlo simulation results are denoted, respectively, by line and points.

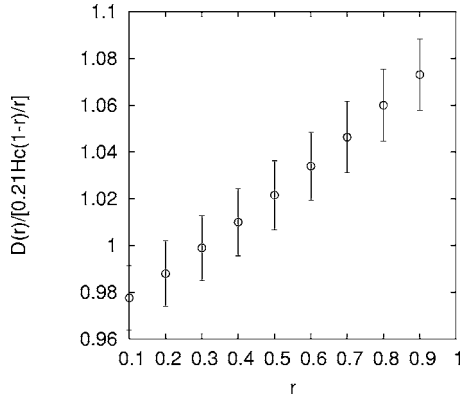

FIG. 4. The diffusion constant $D(r)$ plotted relative to $0.21Hc(1-r)/r$ as a function of intensity reflectance r.

a partial test of the numerical simulations of photon transport presented in the following section.

B. Numerical simulations

To access the photon's random walk in three-dimensional space, we further studied our model by numerical simulations. The computer program takes 10^4 photons at an initial position (on one of the faces of the tetrakaidecahedron), and launches them in a direction specified by polar angles θ and φ. Then it generates the trajectory of each photon following a standard Monte Carlo procedure and evaluates the statistics of the photon cloud at times $\tau \in [500, 650, \ldots, 4850]$ (in units of l/c). The mean-square displacement measuring the width of the photon cloud is computed for each snapshot at time τ, and then fitted to $2D\tau + a_0$ for each spatial direction by the method of linear regression. An offset a_0 takes into account the initial ballistic regime. Within our statistical errors, D_x, D_y, and D_z give the same result and the correlation factors

$$\rho_{xy} = \frac{\langle xy\rangle - \langle x\rangle\langle y\rangle}{\sqrt{\langle x^2\rangle\langle y^2\rangle}},$$

$$\rho_{xz} = \frac{\langle xz\rangle - \langle x\rangle\langle z\rangle}{\sqrt{\langle x^2\rangle\langle z^2\rangle}},$$

$$\rho_{yz} = \frac{\langle yz\rangle - \langle y\rangle\langle z\rangle}{\sqrt{\langle y^2\rangle\langle z^2\rangle}}, \tag{18}$$

are not significant, so the diffusion is isotropic.

For angles $\theta \in [1°, 10°, \ldots, 82°]$, $\varphi \in [90°, 108°, \ldots, 234°]$ and $\theta \in [4°, 13°, \ldots, 85°]$, $\varphi \in [95°, 113°, \ldots, 239°]$ and ten different starting positions, the simulation is repeated for each intensity reflectance $r \in [0.1, 0.2, \ldots, 0.9]$. As a reasonable result, no dependence on the starting point and the starting direction is observed. In Fig. 3 we plot the average of the diffusion constants D_x, D_y, and D_z as a function of r. The line is a fit to $0.21Hc(1-r)/r$. To increase the resolution, the rescaled diffusion constant $D(r)/[0.21Hc(1-r)/r]$ versus r is plotted in Fig. 4. The error bars reflect the standard deviation of an averaging process over all diffusion constants $D(\theta, \varphi)$ for different starting positions and angles. From Fig. 4 we find that our numerical results agree well with the relation

$$D_{\text{Kelvin}}(r) = 0.21Hc\frac{1-r}{r}(1 - b_1 + b_2 r). \tag{19}$$

This is a remarkable result since it demonstrates that for constant reflectance r the diffusion constant of the three-dimensional Kelvin structure and the two-dimensional Voronoi foam [see Eq. (1)] are very similar in spite of the differences in dimension and structure.

IV. PHOTON TRANSPORT IN A KELVIN STRUCTURE: MODEL OF THIN-FILM INTENSITY REFLECTANCE

A. Numerical simulations

In the second, more realistic model, we use the intensity reflectance of thin films. It depends on the polarization state of light, the incident angle (measured with respect to the normal of the film), and the film thickness. It is derived by applying Fresnel's formulas to each liquid-gas interface and summing up multiply reflected light paths in a coherent way [38].

For a plane wave with wave vector $k\hat{\boldsymbol{k}}$ incident from the air onto a liquid film with normal vector $\hat{\boldsymbol{n}}$, the electric field with a general state of polarization is $\boldsymbol{E}_{\text{incident}} = E_x e^{\imath\phi_x}\hat{\boldsymbol{e}}_x + E_y e^{\imath\phi_y}\hat{\boldsymbol{e}}_y + E_z e^{\imath\phi_z}\hat{\boldsymbol{e}}_z$. The plane of incidence is perpendicular to the vector $\hat{\boldsymbol{b}} = \hat{\boldsymbol{n}} \times \hat{\boldsymbol{k}}$. The incident field can be decomposed into a component parallel (p) to the plane of incidence and a component perpendicular (s for the German word "senkrecht") to this plane. For each component, all possible multiple refraction paths in the film are summed up whereby Fresnel's formulas are applied to each refraction event [38]. Ultimately, from this procedure the electric fields of the transmitted and reflected waves are obtained as

$$\boldsymbol{E}_{\text{transmitted}} = (t_s - t_p)(\boldsymbol{E}_{\text{incident}} \cdot \hat{\boldsymbol{b}})\hat{\boldsymbol{b}} + t_p \boldsymbol{E}_{\text{incident}},$$

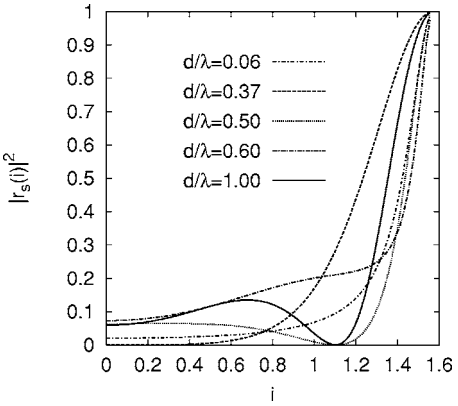

FIG. 5. Intensity reflectance $|r_s|^2$ as a function of angle of incidence i (in radians) for various film thicknesses d/λ as given by Eqs. (B1) and (B2).

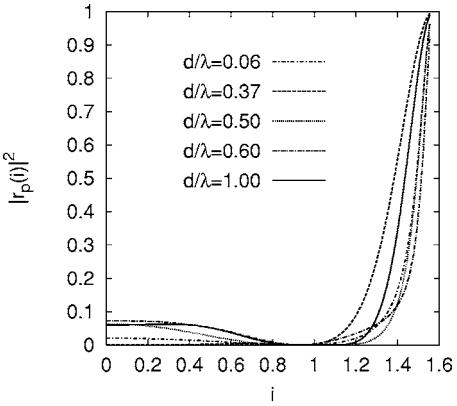

FIG. 6. Intensity reflectance $|r_p|^2$ as a function of angle of incidence i (in radians) for various film thicknesses d/λ as given by Eqs. (B1) and (B2).

$$\boldsymbol{E}_{\text{reflected}} = (r_s + r_p)(\boldsymbol{E}_{\text{incident}} \cdot \hat{\boldsymbol{b}})\hat{\boldsymbol{b}} - r_p \boldsymbol{E}_{\text{incident}} + 2r_p(\boldsymbol{E}_{\text{incident}} \cdot \hat{\boldsymbol{n}})\hat{\boldsymbol{n}}. \tag{20}$$

In Appendix B, the coefficients r_p, t_p, r_s, and t_s are expressed in terms of the incident angle i, film thickness d, light wavelength λ, and film refractive index n_0. The intensity reflectance $r=|\boldsymbol{E}_{\text{reflected}}|^2/|\boldsymbol{E}_{\text{incident}}|^2$ is then obtained from Eq. (20) as

$$r(i) = |r_p|^2 + \frac{|\boldsymbol{E}_{\text{incident}} \cdot \hat{\boldsymbol{b}}|^2}{|\boldsymbol{E}_{\text{incident}}|^2}(|r_s|^2 - |r_p|^2), \tag{21}$$

where $|\,|$ denotes the magnitude of a complex number.

In the limiting cases $\boldsymbol{E}_{\text{incident}} \perp \hat{\boldsymbol{b}}$ and $\boldsymbol{E}_{\text{incident}} \| \hat{\boldsymbol{b}}$, Eq. (21) gives the respective reflectances $|r_s|^2$ and $|r_p|^2$. For perpendicular polarization, Fig. 5 illustrates $r=|r_s|^2$ as a function of the incident angle i for different thicknesses d/λ and the refractive index $n_0=1.34$ of water. For films as thin as a common black film ($d \approx 30$ nm or $d/\lambda=0.06$ for $\lambda=500$ nm), the reflectance is very small but sharply increases to 1 close to grazing incidence ($i=\pi/2$). Increasing the thickness d, oscillations in $r(i)$ start to enter at $d=\lambda/(2n_0)$ due to the constructive and destructive interferences of the multiple refraction paths. For parallel polarization, the reflectance $r=|r_p|^2$ illustrated in Fig. 6 shows a pronounced difference. At Brewster's angle $i_B=\tan^{-1} n_0$, no reflections occur. Moreover, for $i<i_B$ the reflectance is small, it even drops close to zero for d/λ around $1/(2n_0)$. We will see that this feature significantly influences our numerical results on the diffusion of light.

We implemented the full Eqs. (20) and (21) in our Monte Carlo simulations. We used the initial points and launching directions mentioned in Sec. III B, but evaluated the statistics of the photon cloud at times $\tau \in [7000, 7150, \ldots, 11\,500]$ (in units of l/c) in order to achieve the desired accuracy. We did not observe any dependence on the starting point and the starting direction. We, therefore, averaged the simulated diffusion constants over all starting positions and angles, the error bars reflect the standard deviation of this averaging process.

First, we assume that all films of the foam have the same thickness d_{av}. In Fig. 7 we plot the average of the diffusion constants D_x, D_y, and D_z as a function of d_{av}/λ. D is clearly oscillating when d_{av}/λ decreases from 3. It exhibits two strong maxima around $d_{av}/\lambda=0.84$ and 0.43. After a pronounced minimum around $d_{av}/\lambda=0.2$, the diffusion constant finally monotonically increases. Second, in our model we introduce some additional randomness in the thickness of the film d assuming that it is uniformly distributed in $[d_{av}-d_w, d_{av}+d_w]$, where d_{av} denotes the average thickness and d_w the width of the distribution. We will comment on this assumption in Sec. V. In Fig. 8 we plot the diffusion constant as a function of d_{av}/λ for different disorder in the film thickness (for $d_w/d_{av}=0.5$ and 0.9, only data around $d_{av}/\lambda=0.4$ are shown). Obviously, disorder in d decreases the oscillations to an approximately constant diffusion constant D for $d_{av}/\lambda>1$. The two strong maxima are reduced noticeably and ultimately disappear for strong disorder in the film thickness, as illustrated by the data for $d_w/d_{av}=0.5$ and 0.9 around

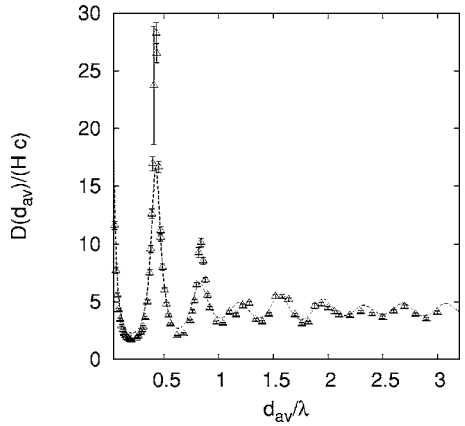

FIG. 7. The diffusion constant in units of cell diameter H times light velocity c as a function of d_{av}/λ for a foam with constant film thickness. Monte Carlo simulation and theoretical results are denoted, respectively, by points and line.

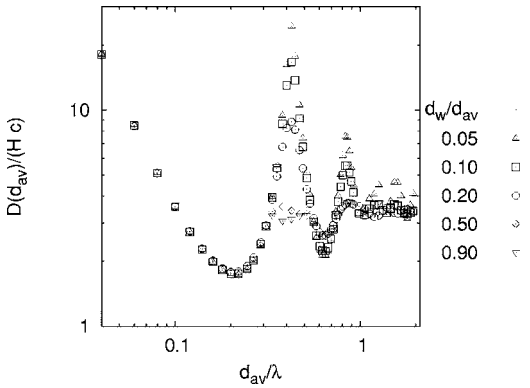

FIG. 8. The diffusion constant in units of cell diameter H times light velocity c as a function of d_{av}/λ for foams with various thickness distribution. Note, for $d_w/d_{av}=0.5$ and 0.9, the pronounced maximum disappears.

$d_{av}/\lambda=0.4$. However, the monotonic increase in D for small d_{av}/λ does not show a significant dependence on d_w.

B. Analytical estimate of the diffusion constant

We now present an analytic theory to calculate the diffusion constant. As mentioned in the Introduction, a multitude of different physical problems have been subsumed under the random-walk concept. In analogy to the freely rotating chain model of polymers [39], one can also evaluate the mean-square displacement of a photon:

$$\langle x^2+y^2+z^2\rangle_n = \left\langle \sum_{i=1}^{n}\sum_{j=1}^{n} \boldsymbol{s}_i\cdot\boldsymbol{s}_j \right\rangle = nl_s^2 + 2l_s^2\sum_{i=1}^{n-1}\sum_{j=i+1}^{n}\left\langle \cos\left(\sum_{k=i+1}^{j}\vartheta_k\right)\right\rangle, \tag{22}$$

where n is the number of random-walk steps and $\boldsymbol{s}_j$ is the jth step vector. In going from the first to the second line, we assume that we can pull out the average step length l_s from the ensemble average. Furthermore, the angle ϑ_k between two adjacent step vectors is introduced. To evaluate the last term in Eq. (22), we apply familiar trigonometric identities, use $\langle\sin\vartheta_k\rangle=0$ valid for nonchiral random walks, and assume the factorization $\langle\cos\vartheta_1\cos\vartheta_2\cdots\cos\vartheta_m\rangle = \langle\cos\vartheta_1\rangle\langle\cos\vartheta_2\rangle\cdots\langle\cos\vartheta_m\rangle$ so that

$$\left\langle \cos\left(\sum_{k=i+1}^{j}\vartheta_k\right)\right\rangle = \langle\cos\vartheta\rangle^{j-i}. \tag{23}$$

The last term in Eq. (22) can now be calculated with the help of the theory for geometrical series and the mean-square displacement finally becomes

$$\langle x^2+y^2+z^2\rangle_n = nl_s^2\frac{1+\langle\cos\vartheta\rangle}{1-\langle\cos\vartheta\rangle}. \tag{24}$$

The time for n steps is $\tau=nl_s/c$, thus comparing to $\langle x^2+y^2+z^2\rangle=6D\tau$ gives an expression for the diffusion constant

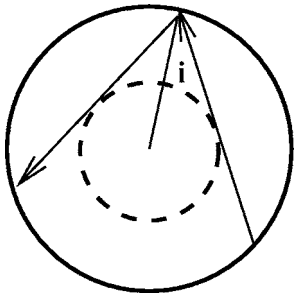

FIG. 9. The cross section of the spheres of radii $H/2$ and $H_i=(H/2)\sin i$ are shown with full and dashed lines, respectively. Any ray tangent to the inner *sphere* leads to the incidence angle i.

$$D=\frac{1}{6}l_s c\frac{1+\langle\cos\vartheta\rangle}{1-\langle\cos\vartheta\rangle}. \tag{25}$$

The task is now to calculate $\langle\cos\vartheta\rangle$. For our foam problem, two contributions arise from photons incident on a liquid film: either $\vartheta=0$ with the probability $t(i)=1-r(i)$ for transmitted photons or $\vartheta=\pi-2i$ with the probability $r(i)$ for reflected photons. Thus

$$\langle\cos\vartheta\rangle = \int_0^{\pi/2}[1-r(i)]w(i)di - \int_0^{\pi/2}\cos(2i)r(i)w(i)di, \tag{26}$$

where $w(i)$ is the probability distribution of the angle of incidence i. Apparently, the magnitude of $\langle\cos\vartheta\rangle$ crucially depends on the distribution $w(i)$.

The probability distribution $w(i)$ can be estimated by approximating the Kelvin cell by a sphere of diameter H. Any incident ray and the center of the sphere define a planar cross section of the sphere, which we show in Fig. 9. Each ray with incident angle i is tangential to an inner sphere with radius $H_i=(H/2)\sin i$. We now assume that the number of rays with incident angles smaller than or equal to i is proportional to the surface $4\pi H_i^2$ of the inner sphere, i.e., the cumulative distribution function $W_c(i)=\int_0^i w(i')di'$ is

$$W_c(i)=\frac{4\pi H_i^2}{4\pi H^2}=\sin(i)^2, \tag{27}$$

and therefore

$$w(i)=\frac{dW_c(i)}{di}=\sin(2i). \tag{28}$$

Figure 10 shows an excellent agreement between Eq. (28) (full line) and Monte Carlo simulations (symbols) confirming our assumption in deriving Eq. (28). As expected, $w(i)$ does not depend on the initial conditions of the photons nor on the value of d_{av}/λ. We checked that the argument to derive $w(i)$ is also valid in two dimensions by replacing the surface of

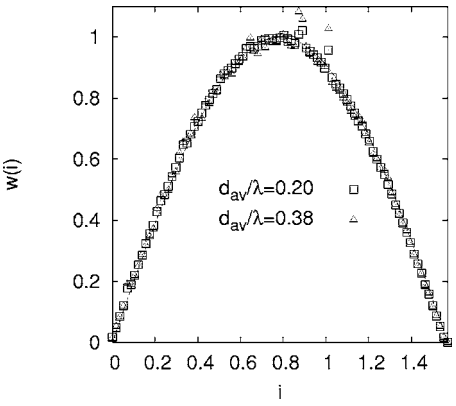

FIG. 10. The probability distribution $w(i)$ (in inverse radians) as a function of i (in radians) for various d_{av}/λ. Monte Carlo simulations (symbols) and theoretical prediction $w(i)=\sin(2i)$ (full line) agree very well.

the inner sphere with the perimeter of an inner circle. This gives a distribution function $w(i)=\cos i$ in agreement with our simulations of photon transport in Voronoi foams [18].

Equation (25) together with Eqs. (26) and (28) represent our analytic theory for the diffusion constant. As reflectance $r(i)$ we take an average over the parallel and perpendicular polarization states of a photon: $r(i)=(|r_p|^2+|r_s|^2)/2$. The result is indicated as a full line in Fig. 7. Clearly, the agreement with our Monte Carlo simulations is excellent. As fit parameter we have chosen $l_s=0.77H$ which is a reasonable value, as the shortest and longest steps are zero and $\sqrt{10}l \approx 1.135H$, respectively.

A closer inspection of Fig. 7 shows that our theory does not fully describe the height of the pronounced maximum at $d_{av}/\lambda=0.43$. The reason lies in the reflectance $r(i)$ which we choose as an average over $|r_p|^2$ and $|r_s|^2$. By doing this, we neglect long straight photon paths that cross parallel faces in the Kelvin structure. They occur for the parallel polarization state since below the Brewster angle the reflectance is small and in the case of $d_{av}/\lambda=0.43$ close to zero [see Fig. 6]. We have explicitly confirmed this explanation in the two-dimensional case where parallel and perpendicular polarization states do not mix. When we bring disorder into the foam, parallel faces no longer exist and the height of the maximum will decrease to the value predicted by our theoretical approach.

V. DISCUSSIONS AND CONCLUSIONS

In previous papers, we have investigated photon transport in two-dimensional model foams [17–19]. To extend our investigations to three dimensions, we have studied persistent random walks on a Kelvin structure based on rules motivated by ray optics. Although the Kelvin foam is a highly idealized periodic structure, it serves as a first legitimate approach for understanding diffusion of light in three-dimensional foams. In a first model, we used a constant intensity reflectance r. We identified special cases where photons move on a line (1D random walk) or in a plane (2D random walk) and derived the corresponding diffusion constants analytically [see Eqs. (4) and (17)]. In general, photons diffuse in three-dimensional space, thus we performed numerical simulations to mimic their random walks and determined the diffusion constant (19). Quite remarkably, the diffusion constants of the 3D Kelvin structure and 2D disordered Voronoi foams are very similar [see Eqs. (19) and (1)]. This confirms our speculation in Ref. [18] that the dimension of space does not have a strong influence on the magnitude of the diffusion constant. Note that in all these cases, the diffusion constant is mainly controlled by the factor $(1-r)/r$ independent of the dimension of space and the cell's shape. It expresses the fact that for $r=0$ photon transport is ballistic and that for $r=1$ photons stay confined to the initial cell.

Several features of our results are remarkable. Apart from a few cases discussed in Secs. II and III A, the diffusion constant does not depend on the injection angles. Furthermore, it deviates from the $(1-r)/r$ law by an additional factor linear in r. This is clearly visible in Fig. 4. So features of the 2D disordered Voronoi foams are preserved in the three-dimensional case [18]. This indicates that the special photon paths in our ordered 3D foam, as discussed in Sec. II, are not important for the overall diffusion constant, in contrast to the 2D hexagonal foam [17]. Furthermore, our current guess is that the additional linear factor represents path correlations induced by the local structure of the foam [19]. The presence of such correlations is clear when *all* faces are reflecting ($r=1$), as highly correlated succesive reflections ensure the photon confinement.

In a second, more realistic model, we used the intensity reflectances of thin films illustrated in Figs. 5 and 6. They show a very rich dependence on film thickness and angle of incidence. Their common characteristic feature is that close to grazing incidence ($i=\pi/2$), the reflectance always sharply increases to one, which means total reflection even for films as thin as the common black film. We performed extensive Monte Carlo simulations using these thin-film reflectances. The diffusion constant exhibits oscillations when plotted as a function of film thickness and then steadily increases for $d_{av}/\lambda<0.2$. When disorder is introduced in the film thickness, the oscillations disappear whereas the steady increase remains unaltered. We are able to model the photons' random walk and calculate the diffusion constant with a theory in analogy to the rotating chain model of polymers. Besides an average reflectance and a mean-step length, the theory requires a distribution function for the angle of incidence for which we motivate an analytic formula in accord with simulations. The theory gives an excellent agreement with the simulation data. It extends our qualitative explanation of the diffusion constant based on incident-angle averaged reflection coefficients in Ref. [18]. Our "mean-field" theory does not fully describe the height of the most pronounced maximum in Fig. 7. We attribute this feature to the very small reflectance in the parallel polarization state when the incident angles are smaller than or equal to the Brewster angle. The extreme height is an artifact of the Kelvin structure, it should be reduced in disordered foams even without disorder in the film thickness. Note that parallel polarized light propagating through one-dimensional disordered structures also exhibits a Brewster anomaly since localization lengths become ex-

tremely large [40]. Nevertheless, the strength of our analytic theory is that it gives a reliable estimate of the diffusion constant using a minimum of input parameters and a distribution function for the angle of incidence that encodes the foam structure. We add here a comment about our model foam. As already mentioned in the beginning of Sec. II, the unit cell of the Kelvin foam is actually the tetrakaidecahedron with some small curvature added to the hexagonal faces. This curvature will not change the distribution function $w(i)$ of Eq. (28) significantly and we, therefore, do not expect any significant changes in the diffusion coefficient.

Careful measurements of the diffusion constant as a function of the liquid volume fraction ε were performed by Vera, Saint-Jalmes, and Durian [9]. To compare our theoretical findings to their experiments, we should know how the film thickness d_{av} depends on ε. However, there are controversial statements in literature. On the one hand, it is assumed that d_{av} is set by the interfacial forces, i.e., independent of ε. Even for this situation, different values are stated with $d_{av} \approx 30$ nm (common black film) [41,42] and $d_{av} \approx 100$ nm [43]. On the other hand, a linear relationship $d_{av} \propto \varepsilon$ is reported with film thicknesses up to 2000 nm [44]. The last reference might also justify our assumption that the film thickness in a real foam shows some distribution about an average value. By such a mechanism, we reduce the oscillations in the diffusion constant to a nearly constant value for $d_{av}/\lambda > 0.2$ when plotted against the ratio d_{av}/λ of film thickness to wavelength of light. This might be one explanation that in experiments only a weak dependence of the diffusion constant on λ is observed [9]. Another explanation is that thin-film reflectances, as employed in this paper, are not important in the experiments just reported. Indeed recent experiments observe photon channeling in the range $0.04 < \varepsilon < 0.2$ for the liquid volume fraction [20]. This phenomena can be explained by treating reflections and transmittances at each liquid-gas interface separately without taking into account interferences between light rays as it is done for thin films [45]. Our current view is [45] that the work presented here applies to very dry foams with $\varepsilon < 0.04$ where photon channeling is absent [20]. Especially, by taking into account thin-film reflectances, our model is able to explain the divergence of the diffusion constant D with decreasing ε, as observed in experiments [9], whereas the photon-channeling model gives a constant D for $\varepsilon \to 0$ [45].

In experiments, the transport-mean-free path l^* is measured as the key parameter of diffusive light transport [4–6]. In three-dimensional systems, it is defined via $D = cl^*/3$. Experimental values for l^*/H increase from 2 to 20 for decreasing ε [9] whereas we determine a range of l^*/H between 10 (for $d_{av}/\lambda > 0.8$) and 25 (for $d_{av}/\lambda = 0.06$, i.e., for a common black film) as illustrated in Fig. 8. That means our theoretical values for l^* fall in the same range as the experimental values for the driest foams in Ref. [9]. This shows that liquid films are important for the understanding of photon diffusion in dry foams otherwise we should have obtained much larger transport-mean-free paths.

The Kelvin structure is an idealized foam. We, therefore, are extending our studies towards real dry foams by introducing topological and geometrical disorder based on a 3D Voronoi-foam model. This will provide us with a pretty realistic system which will enable us to study, e.g., whether random orientations of the liquid films decrease the transport-mean-free path as observed in the two-dimensional case [18]. Further extensions of the model would then include scattering from Plateau borders and vertices.

Gradually our understanding of diffusive light transport is evolving. For medium liquid volume fraction, photon channeling seems to be a very appealing model. For very dry foams, the importance of ray optics together with thin-film reflectances could be checked. For example, close to a common black film, the diffusion constant should exhibit a strong dependence on the wavelength of light. Another path to pursue is the creation of artificial foam structures which would help to systematically test the influence of various parameters on photon diffusion. So, to achieve a complete understanding of photon diffusion in foams, there is still much to do for both experimentalists and theorists.

ACKNOWLEDGMENTS

We would like to thank D. J. Durian, J. Guck, R. Höhler, J. Kaes, G. Maret, C. Quilliet, N. Rivier, and Z. Sadjadi for fruitful discussions. We also thank Iran's Ministry of Science, Research and Technology for support of the parallel computing facilities at IASBS under Grant No. 1026B (503495). MF.M. appreciates financial support from Iran Telecommunication Research Center (ITRC). H.S. acknowledges financial support from the Deutsche Forschungsgemeinschaft under Grant No. Sta 352/5-1. MF.M. and H.S. thank the International Graduate College "Soft Matter" at the University of Konstanz for financial support.

APPENDIX A

The tetrakaidecahedral cell has six square faces which we number from 1 to 6. The remaining faces are hexagons which we number from 7 to 14. The origin of the Cartesian coordinates is placed at the center of the unit cell, and unit vectors $\hat{\boldsymbol{e}}_x$, $\hat{\boldsymbol{e}}_y$, and $\hat{\boldsymbol{e}}_z$ are assumed normal to faces 1, 2, and 6, respectively. Note that the third (fourth) (sixth) face is obtained by reflecting the first (second) (fifth) face in the plane $x=0 (y=0)(z=0)$. Eleventh, twelfth, thirteenth, and fourteenth faces are reflections of the eighth, ninth, tenth, and seventh faces, respectively, in the origin $(x=y=z=0)$.

In Table I, the ith face is characterized by its center $\boldsymbol{c}_i$, its normal vector $\hat{\boldsymbol{n}}_i$, and its set of vertices $\{\boldsymbol{v}_i^1, \boldsymbol{v}_i^2, \boldsymbol{v}_i^3, \boldsymbol{v}_i^4\}$ or $\{\boldsymbol{v}_i^1, \boldsymbol{v}_i^2, \boldsymbol{v}_i^3, \boldsymbol{v}_i^4, \boldsymbol{v}_i^5, \boldsymbol{v}_i^6\}$. l denotes the cell edge length and $a = 2\sqrt{2}l$.

The conventional unit cell of a bcc structure contains two lattice points. By definition, the Voronoi cell of a bcc structure contains one lattice point. It follows that the volume of the tetrakaidecahedral cell is $a^3/2$. We define the effective diameter H of the cell through the relation $\pi H^3/6 = a^3/2$ or

$$H = \sqrt[3]{\frac{48\sqrt{2}}{\pi}} l \approx 2.78528l. \tag{A1}$$

TABLE I. Characteristics of the tetrakaidecahedral cell.

Face	$\boldsymbol{c}_i$	$\hat{\boldsymbol{n}}_i$	$\boldsymbol{v}_i^j$
1	$\left(\frac{1}{2},0,0\right)a$	(1,0,0)	$\boldsymbol{v}_1^1=\left(\frac{1}{2},0,\frac{1}{4}\right)a$ $\boldsymbol{v}_1^2=\left(\frac{1}{2},\frac{1}{4},0\right)a$ $\boldsymbol{v}_1^3=\left(\frac{1}{2},0,-\frac{1}{4}\right)a$ $\boldsymbol{v}_1^4=\left(\frac{1}{2},-\frac{1}{4},0\right)a$
2	$\left(0,\frac{1}{2},0\right)a$	(0,1,0)	$\boldsymbol{v}_2^1=\left(0,\frac{1}{2},\frac{1}{4}\right)a$ $\boldsymbol{v}_2^2=\left(\frac{1}{4},\frac{1}{2},0\right)a$ $\boldsymbol{v}_2^3=\left(0,\frac{1}{2},-\frac{1}{4}\right)a$ $\boldsymbol{v}_2^4=\left(-\frac{1}{4},\frac{1}{2},0\right)a$
3	$\left(-\frac{1}{2},0,0\right)a$	(−1,0,0)	$\boldsymbol{v}_3^1=\left(-\frac{1}{2},0,\frac{1}{4}\right)a$ $\boldsymbol{v}_3^2=\left(-\frac{1}{2},\frac{1}{4},0\right)a$ $\boldsymbol{v}_3^3=\left(-\frac{1}{2},0,-\frac{1}{4}\right)a$ $\boldsymbol{v}_3^4=\left(-\frac{1}{2},-\frac{1}{4},0\right)a$
4	$\left(0,-\frac{1}{2},0\right)a$	(0,−1,0)	$\boldsymbol{v}_4^1=\left(0,-\frac{1}{2},\frac{1}{4}\right)a$ $\boldsymbol{v}_4^2=\left(\frac{1}{4},-\frac{1}{2},0\right)a$ $\boldsymbol{v}_4^3=\left(0,-\frac{1}{2},-\frac{1}{4}\right)a$ $\boldsymbol{v}_4^4=\left(-\frac{1}{4},-\frac{1}{2},0\right)a$
5	$\left(0,0,-\frac{1}{2}\right)a$	(0,0,−1)	$\boldsymbol{v}_5^1=\left(\frac{1}{4},0,-\frac{1}{2}\right)a$ $\boldsymbol{v}_5^2=\left(0,\frac{1}{4},-\frac{1}{2}\right)a$ $\boldsymbol{v}_5^3=\left(-\frac{1}{4},0,-\frac{1}{2}\right)a$ $\boldsymbol{v}_5^4=\left(0,-\frac{1}{4},-\frac{1}{2}\right)a$
6	$\left(0,0,\frac{1}{2}\right)a$	(0,0,1)	$\boldsymbol{v}_6^1=\left(\frac{1}{4},0,\frac{1}{2}\right)a$ $\boldsymbol{v}_6^2=\left(0,\frac{1}{4},\frac{1}{2}\right)a$ $\boldsymbol{v}_6^3=\left(-\frac{1}{4},0,\frac{1}{2}\right)a$ $\boldsymbol{v}_6^4=\left(0,-\frac{1}{4},\frac{1}{2}\right)a$
7	$\left(\frac{1}{4},\frac{1}{4},\frac{1}{4}\right)a$	$\left(\frac{1}{\sqrt{3}},\frac{1}{\sqrt{3}},\frac{1}{\sqrt{3}}\right)$	$\boldsymbol{v}_7^1=\left(\frac{1}{2},\frac{1}{4},0\right)a$ $\boldsymbol{v}_7^2=\left(\frac{1}{4},\frac{1}{2},0\right)a$ $\boldsymbol{v}_7^3=\left(0,\frac{1}{2},\frac{1}{4}\right)a$ $\boldsymbol{v}_7^4=\left(0,\frac{1}{4},\frac{1}{2}\right)a$ $\boldsymbol{v}_7^5=\left(\frac{1}{4},0,\frac{1}{2}\right)a$ $\boldsymbol{v}_7^6=\left(\frac{1}{2},0,\frac{1}{4}\right)a$
8	$\left(-\frac{1}{4},\frac{1}{4},\frac{1}{4}\right)a$	$\left(-\frac{1}{\sqrt{3}},\frac{1}{\sqrt{3}},\frac{1}{\sqrt{3}}\right)$	$\boldsymbol{v}_8^1=\left(0,\frac{1}{2},\frac{1}{4}\right)a$ $\boldsymbol{v}_8^2=\left(0,\frac{1}{4},\frac{1}{2}\right)a$ $\boldsymbol{v}_8^3=\left(-\frac{1}{2},\frac{1}{4},0\right)a$ $\boldsymbol{v}_8^4=\left(-\frac{1}{4},\frac{1}{2},0\right)a$ $\boldsymbol{v}_8^5=\left(-\frac{1}{2},0,\frac{1}{4}\right)a$ $\boldsymbol{v}_8^6=\left(-\frac{1}{4},0,\frac{1}{2}\right)a$
9	$\left(-\frac{1}{4},-\frac{1}{4},\frac{1}{4}\right)a$	$\left(-\frac{1}{\sqrt{3}},-\frac{1}{\sqrt{3}},\frac{1}{\sqrt{3}}\right)$	$\boldsymbol{v}_9^1=\left(-\frac{1}{2},0,\frac{1}{4}\right)a$ $\boldsymbol{v}_9^2=\left(-\frac{1}{2},-\frac{1}{4},0\right)a$ $\boldsymbol{v}_9^3=\left(-\frac{1}{4},-\frac{1}{2},0\right)a$ $\boldsymbol{v}_9^4=\left(0,-\frac{1}{2},\frac{1}{4}\right)a$ $\boldsymbol{v}_9^5=\left(0,-\frac{1}{4},\frac{1}{2}\right)a$ $\boldsymbol{v}_9^6=\left(-\frac{1}{4},0,\frac{1}{2}\right)a$
10	$\left(\frac{1}{4},-\frac{1}{4},\frac{1}{4}\right)a$	$\left(\frac{1}{\sqrt{3}},-\frac{1}{\sqrt{3}},\frac{1}{\sqrt{3}}\right)$	$\boldsymbol{v}_{10}^1=\left(\frac{1}{2},0,\frac{1}{4}\right)a$ $\boldsymbol{v}_{10}^2=\left(\frac{1}{2},-\frac{1}{4},0\right)a$ $\boldsymbol{v}_{10}^3=\left(0,-\frac{1}{2},\frac{1}{4}\right)a$ $\boldsymbol{v}_{10}^4=\left(\frac{1}{4},-\frac{1}{2},0\right)a$ $\boldsymbol{v}_{10}^5=\left(\frac{1}{4},0,\frac{1}{2}\right)a$ $\boldsymbol{v}_{10}^6=\left(0,-\frac{1}{4},\frac{1}{2}\right)a$
11	$\left(\frac{1}{4},-\frac{1}{4},-\frac{1}{4}\right)a$	$\left(\frac{1}{\sqrt{3}},-\frac{1}{\sqrt{3}},-\frac{1}{\sqrt{3}}\right)$	$\boldsymbol{v}_{11}^1=\left(0,-\frac{1}{2},-\frac{1}{4}\right)a$ $\boldsymbol{v}_{11}^2=\left(0,-\frac{1}{4},-\frac{1}{2}\right)a$

TABLE I. (*Continued.*)

Face	$\boldsymbol{c}_i$	$\hat{\boldsymbol{n}}_i$	$\boldsymbol{v}_i^j$
			$\boldsymbol{v}_{11}^3=\left(\frac{1}{2},-\frac{1}{4},0\right)a$ $\boldsymbol{v}_{11}^4=\left(\frac{1}{4},-\frac{1}{2},0\right)a$
			$\boldsymbol{v}_{11}^5=\left(\frac{1}{2},0,-\frac{1}{4}\right)a$ $\boldsymbol{v}_{11}^6=\left(\frac{1}{4},0,-\frac{1}{2}\right)a$
12	$\left(\frac{1}{4},\frac{1}{4},-\frac{1}{4}\right)a$	$\left(\frac{1}{\sqrt{3}},\frac{1}{\sqrt{3}},-\frac{1}{\sqrt{3}}\right)$	$\boldsymbol{v}_{12}^1=\left(\frac{1}{2},0,-\frac{1}{4}\right)a$ $\boldsymbol{v}_{12}^2=\left(\frac{1}{2},\frac{1}{4},0\right)a$
			$\boldsymbol{v}_{12}^3=\left(\frac{1}{4},\frac{1}{2},0\right)a$ $\boldsymbol{v}_{12}^4=\left(0,\frac{1}{2},-\frac{1}{4}\right)a$
			$\boldsymbol{v}_{12}^5=\left(0,\frac{1}{4},-\frac{1}{2}\right)a$ $\boldsymbol{v}_{12}^6=\left(\frac{1}{4},0,-\frac{1}{2}\right)a$
13	$\left(-\frac{1}{4},\frac{1}{4},-\frac{1}{4}\right)a$	$\left(-\frac{1}{\sqrt{3}},\frac{1}{\sqrt{3}},-\frac{1}{\sqrt{3}}\right)$	$\boldsymbol{v}_{13}^1=\left(-\frac{1}{2},0,-\frac{1}{4}\right)a$ $\boldsymbol{v}_{13}^2=\left(-\frac{1}{2},\frac{1}{4},0\right)a$
			$\boldsymbol{v}_{13}^3=\left(0,\frac{1}{2},-\frac{1}{4}\right)a$ $\boldsymbol{v}_{13}^4=\left(-\frac{1}{4},\frac{1}{2},0\right)a$
			$\boldsymbol{v}_{13}^5=\left(-\frac{1}{4},0,-\frac{1}{2}\right)a$ $\boldsymbol{v}_{13}^6=\left(0,\frac{1}{4},-\frac{1}{2}\right)a$
14	$\left(-\frac{1}{4},-\frac{1}{4},-\frac{1}{4}\right)a$	$\left(-\frac{1}{\sqrt{3}},-\frac{1}{\sqrt{3}},-\frac{1}{\sqrt{3}}\right)$	$\boldsymbol{v}_{14}^1=\left(-\frac{1}{2},-\frac{1}{4},0\right)a$ $\boldsymbol{v}_{14}^2=\left(-\frac{1}{4},-\frac{1}{2},0\right)a$
			$\boldsymbol{v}_{14}^3=\left(0,-\frac{1}{2},-\frac{1}{4}\right)a$ $\boldsymbol{v}_{14}^4=\left(0,-\frac{1}{4},-\frac{1}{2}\right)a$
			$\boldsymbol{v}_{14}^5=\left(-\frac{1}{4},0,-\frac{1}{2}\right)a$ $\boldsymbol{v}_{14}^6=\left(-\frac{1}{2},0,-\frac{1}{4}\right)a$

Note: $\boldsymbol{c}_i$, $\hat{\boldsymbol{n}}_i$, and $\boldsymbol{v}_i^j$ are center, normal vector, and vertices of the ith face, respectively. l denotes the cell edge length and $a=2\sqrt{2}l$.

APPENDIX B

The coeffients r_p, r_s, t_p, and t_s introduced in Eq. (20) are

$$r_p=\frac{r_{12p}(1-e^{\imath\beta})}{1-r_{12p}^2e^{\imath\beta}},$$

$$t_p=\frac{t_{12p}t_{23p}e^{\imath\beta/2}}{1-r_{12p}^2e^{\imath\beta}},$$

$$r_s=\frac{r_{12s}(1-e^{\imath\beta})}{1-r_{12s}^2e^{\imath\beta}},$$

$$t_s=\frac{t_{12s}t_{23s}e^{\imath\beta/2}}{1-r_{12s}^2e^{\imath\beta}}, \tag{B1}$$

where

$$r_{12p}=\frac{n_0^2\cos i-\sqrt{n_0^2-\sin^2 i}}{n_0^2\cos i+\sqrt{n_0^2-\sin^2 i}},$$

$$t_{12p}=\frac{2n_0\cos i}{n_0^2\cos i+\sqrt{n_0^2-\sin^2 i}},$$

$$t_{23p}=\frac{2n_0\sqrt{n_0^2-\sin^2 i}}{n_0^2\cos i+\sqrt{n_0^2-\sin^2 i}},$$

$$r_{12s}=\frac{\cos i-\sqrt{n_0^2-\sin^2 i}}{\cos i+\sqrt{n_0^2-\sin^2 i}},$$

$$t_{12s}=\frac{2\cos i}{\cos i+\sqrt{n_0^2-\sin^2 i}},$$

$$t_{23s}=\frac{2\sqrt{n_0^2-\sin^2 i}}{\cos i+\sqrt{n_0^2-\sin^2 i}},$$

$$\beta=4\pi\frac{d}{\lambda}\sqrt{n_0^2-\sin^2(i)}. \tag{B2}$$

[1] *Scattering and Localization of Classical Waves in Random Media*, edited by P. Sheng (World Scientific, Singapore, 1990); P. Sheng, *Introduction to Wave Scattering, Localization, and Mesoscopic Phenomena* (Academic Press, San Diego, 1995).
[2] G. Maret, in *Mesoscopic Quantum Physics, Proceedings of the Les Houches Summer School*, Session LXI, 1994, edited by E. Akkermans, G. Montambaux, J.-L. Pichard, and J. Zinn-Justin (North-Holland, Amsterdam, 1995).
[3] B. A. van Tiggelen, R. Maynard, and A. Heiderich, Phys. Rev. Lett. **77**, 639 (1996); H. Stark and T. C. Lubensky, *ibid.* **77**, 2229 (1996); B. van Tiggelen and H. Stark, Rev. Mod. Phys. **72**, 1017 (2000).
[4] G. Maret and P. E. Wolf, Z. Phys. B: Condens. Matter **65**, 409 (1987); G. Maret, Curr. Opin. Colloid Interface Sci. **2**, 251 (1997).
[5] D. J. Pine, D. A. Weitz, P. M. Chaikin, and E. Herbolzheimer, Phys. Rev. Lett. **60**, 1134 (1988).
[6] P. D. Kaplan, A. D. Dinsmore, A. G. Yodh, and D. J. Pine, Phys. Rev. E **50**, 4827 (1994).
[7] D. J. Durian, D. A. Weitz, and D. J. Pine, Science **252**, 686 (1991).
[8] D. J. Durian, D. A. Weitz, and D. J. Pine, Phys. Rev. A **44**, R7902 (1991).
[9] M. U. Vera, A. Saint-Jalmes, and D. J. Durian, Appl. Opt. **40**, 4210 (2001).
[10] J. C. Earnshaw and A. H. Jaafar, Phys. Rev. E **49**, 5408 (1994).
[11] R. Höhler, S. Cohen-Addad, and H. Hoballah, Phys. Rev. Lett. **79**, 1154 (1997).
[12] S. Cohen-Addad and R. Höhler, Phys. Rev. Lett. **86**, 4700 (2001).
[13] A. D. Gopal and D. J. Durian, J. Colloid Interface Sci. **213**, 169 (1999).
[14] S. Cohen-Addad, R. Höhler, and Y. Khidas, Phys. Rev. Lett. **93**, 028302 (2004).
[15] D. Weaire and S. Hutzler, *The Physics of Foams* (Oxford University Press, New York, 1999).
[16] S. Skipetrov (unpublished).
[17] M. F. Miri and H. Stark, Phys. Rev. E **68**, 031102 (2003).
[18] M. F. Miri and H. Stark, Europhys. Lett. **65**, 567 (2004).
[19] M. F. Miri and H. Stark, J. Phys. A **38**, 3743 (2005).
[20] A. S. Gittings, R. Bandyopadhyay, and D. J. Durian, Europhys. Lett. **65**, 414 (2004).
[21] G. H. Weiss, *Aspects and Applications of the Random Walk* (North-Holland, Amsterdam, 1994).
[22] J. W. Haus and K. W. Kehr, Phys. Rep. **150**, 263 (1987).
[23] R. Fürth, Ann. Phys. **53**, 177 (1917).
[24] G. I. Taylor, Proc. London Math. Soc. **20**, 196 (1921).
[25] P. J. Flory, *Statistical Mechanics of Chain Molecules* (Interscience, New York, 1969).
[26] M. E. Glicksman, *Diffusion in Solids: Field Theory, Solid-State Principles, and Applications* (Wiley, New York, 2000).
[27] D. J. Bicout and I. Sache, Phys. Rev. E **67**, 031913 (2003).
[28] R. Sambeth and A. Baumgaertner, Phys. Rev. Lett. **86**, 5196 (2001).
[29] H. Larralde, Phys. Rev. E **56**, 5004 (1997).
[30] M. Boguñá, J. M. Porrà, and J. Masoliver, Phys. Rev. E **58**, 6992 (1998).
[31] M. Boguñá, J. M. Porrà, and J. Masoliver, Phys. Rev. E **59**, 6517 (1999).
[32] D. Weaire and N. Rivier, Contemp. Phys. **25**, 59 (1984).
[33] A. Okabe, B. Boots, and K. Sugihara, *Spatial Tessellations: Concepts and Applications of Voronoi Diagrams* (Wiley, Chichester, 1992).
[34] A. M. Kraynik, and D. A. Reinelt, J. Colloid Interface Sci. **181**, 511 (1996); Forma **11**, 255 (1996); D. A. Reinelt and A. M. Kraynik, J. Colloid Interface Sci. **159**, 460 (1996); J. Fluid Mech. **311**, 327 (1996); H. X. Zhu, J. F. Knott, and N. J. Mills, J. Mech. Phys. Solids **45**, 319 (1997); W. E. Warren and A. M. Kraynik, J. Appl. Mech. **64**, 787 (1997).
[35] D. Weaire and R. Phelan, Philos. Mag. Lett. **69**, 107 (1994).
[36] N. Rivier, Philos. Mag. Lett. **69**, 297 (1994).
[37] *The Kelvin Problem*, edited by D. Weaire (Taylor & Francis, London, 1996).
[38] J. R. Reitz, F. J. Milford, and R. W. Christy, *Foundations of Electromagnetic Theory* (Addison-Wesley, Reading, 1979).
[39] M. Doi and S. F. Edwards, *The Theory of Polymer Dynamics* (Oxford University Press, New York, 1986).
[40] J. E. Sipe, P. Sheng, B. S. White, and M. H. Cohen, Phys. Rev. Lett. **60**, 108 (1988).
[41] C. Monnereau and M. Vignes-Adler, Phys. Rev. Lett. **80**, 5228 (1998).
[42] S. Hilgenfeldt, S. A. Koehler, and H. A. Stone, Phys. Rev. Lett. **86**, 4704 (2001).
[43] M. U. Vera and D. J. Durian, Phys. Rev. Lett. **88**, 088304 (2002).
[44] V. Carrier, S. Destouesse, and A. Colin, Phys. Rev. E **65**, 061404 (2002).
[45] M. Schmiedeberg, M. F. Miri, and H. Stark, Eur. Phys. J. E., cond-mat/0505406.